Available online at www.sciencedirect.com

SciVerse ScienceDirect

Ceramics International 38 (2012) 4885–4893

CERAMICS INTERNATIONAL

www.elsevier.com/locate/ceramint

Modification of electrophoretically deposited nano-hydroxyapatite coatings by wire brushing on Ti–6Al–4V substrates

Hamidreza Farnoush [a], Jamshid Aghazadeh Mohandesi [a,*], Davoud Haghshenas Fatmehsari [a], Fathollah Moztarzadeh [b]

[a] Department of Mining and Metallurgical Engineering, Amirkabir University of Technology, P.O. Box 15875-4413, Tehran, Iran
[b] Biomedical Engineering Department, Amirkabir University of Technology, P.O. Box 15875-4413, Tehran, Iran

Received 15 February 2012; received in revised form 24 February 2012; accepted 24 February 2012
Available online 5 March 2012

Abstract

In the present study, after successful synthesis of nano-HA powders by chemical precipitation method, wire-brushing (WB) treatment was effectively employed on Ti–6Al–4V substrates for the modification of electrophoretically deposited nano-hydroxyapatite coatings. The precipitated nano-HA particles were characterized by XRD, FT-IR, and DLS analyses. The morphology and particle size of synthesized nano-HA particles was observed by FE-SEM. The Ti–6Al–4V plates were initially wire brushed at different times and rotational speeds. Microhardness profile and AFM analysis of substrates were then studied. It was found that WB treatment at 16,000 rpm for 60 s leads to a maximum enhancement in the hardness and roughness of surface. Then, the electrophoretic deposition of nano-HA particles was carried out at constant voltage of 30 V and after 60 s. The results of adhesion test and potentiodynamic polarization measurements showed that WB treatment on Ti–6Al–4V substrates could efficiently increase the bonding strength between coating and substrate as well as corrosion resistance.

Keywords: A. Powders: chemical preparation; B. Surfaces; C. Strength; D. Apatite; E. Biomedical applications; Electrophoretic deposition

1. Introduction

Titanium and its alloy have been widely utilized in biomaterial applications due to their relatively excellent corrosion resistance, favorable biocompatibility, and high specific strength (strength per density) [1]. Regarding the poor osteoinductive properties of Ti, the use of hydroxyapatite (HA, $Ca_{10}(PO_4)_6(OH)_2$) coatings has received considerable attention [2]. On the other hand, HA is a very brittle bioactive ceramic material and the fabrication of HA coatings on tough metallic substrates take the advantages of both mechanical properties of metal substrates and biological performances of HA ceramics [2]. Among different techniques employed for preparing HA coatings on a metallic substrate, such as plasma spray [3,4], sol–gel [5,6], biomimetic [7,8] and ion implantation [9], electrophoretic deposition (EPD) [10,11] is an effective technique for the fabrication of dense and uniform HA coatings even on the substrates with complex geometries. This technique has the advantages of high production rate and low investment cost [12]. However, the poor adhesion strength between HA coating and Ti substrate limits its clinical application [12].

In fabrication process of Ti/HA coatings, due to degradation of metallic substrate and decomposition of HA, sintering temperatures should be below 1000 °C under which HA is difficult to be fully densified [13–15]. Furthermore, the thermal expansion coefficient of titanium substrate is much lower than that of HA [16–18], and the thermal contraction mismatch results in the formation of cracks when cooled from the elevated temperatures; Also, a significant firing shrinkage during sintering results in the formation of cracks in coatings as well [19].

Mechanical surface modification methods, such as machining [20,21], polishing [22,23], and blasting [24–27], is typically implemented for achieving specific surface topographies and roughness, removing surface contamination, and/or improving adhesion in subsequent bonding steps. Wire brushing (WB), another mechanical surface modification technique, removes surface contaminated layers and oxide layers. More importantly,

---

* Corresponding author. Tel.: +98 21 64542949; fax: +98 21 64542941.
E-mail addresses: farnoush@aut.ac.ir (H. Farnoush), jamshidaghazadeh@gmail.com (J. Aghazadeh Mohandesi).

0272-8842/$36.00 © 2012 Elsevier Ltd and Techna Group S.r.l. All rights reserved.
doi:10.1016/j.ceramint.2012.02.079

it forms a hardened cover layer on the surface [28,29] and increases the surface roughness. Since the bonding strength of HA coating is substantially affected by the surface roughness of the substrate [30,31], this method can be potentially applied for the modification of electrophoretically deposited nano-hydroxyapatite coatings. To the authors' best knowledge, there is no through work reporting the influence of WB treatment on the bonding strength of HA coatings.

The present work addresses a fairly complete investigation of the effect of WB treatment on the bonding strength of nano-HA coatings. The optimum WB parameters (i.e. rotational speed and time) were chosen by microhardness and roughness analyses on the WB-treated Ti–6Al–4V substrates. Then, the electrophoretic deposition of synthesized nano-HA particles was studied in the ethanol-based suspension. Finally, the electrochemical corrosion behavior in SBF (simulated body fluid) solution and bonding strength of WB-treated and as-received samples were discussed.

2. Experimental procedures

2.1. Synthesis of nano-HA powders

Nanocrystalline hydroxyapatite powders were synthesized by precipitation method using $Ca(NO_3)_2{\cdot}4H_2O$ (CNT, Merck No. 141231) and $(NH_4)_2HPO_4$ (PHA, Merck No. 21,599-6) as starting precursors and ammonia solution for pH adjustment. Firstly, 0.29 M CNT and 0.24 M PHA solutions were separately prepared in double distilled water. Then, PHA solution was slowly added dropwise to the CNT solution. In all experiments the pH of CNT solution was 11. The suspension was heated to 80 °C, rigorously stirred for 1 h, and finally kept for 24 h of ageing at room temperature. The HA precipitate was then washed by thrice repeating the following three steps: centrifugation at the rotation speed of 3000 rpm, supernatant decantation, and re-suspension in de-ionized water. The gel obtained was dried at 65 °C for 24 h in a dry oven and calcined at 900 °C for 1 h. The structure of the resulting powder after drying was evaluated by Fourier transform infrared (FTIR, Nicolet Nexus 670) spectroscopy in the wave number range of 4000–400 cm^{-1}. The phase transformation during heat treatment and crystallite size evolutions were carried out by X-ray diffraction analysis (XRD, Philips PW 1480) with Cu K_α radiation ($\lambda = 1.5405$ Å). The Scherrer method was used to estimate the crystallite size. The size and morphology of the precipitated HA nano-particles were assessed by field-emission scanning electron microscopy (FE-SEM, Hitachi S-4160).

2.2. Wire brushing of Ti–6Al–4V substrates

The as-received material (AR) was 3-mm-thick mill-annealed Ti–6Al–4V plates with the chemical composition of Al 6.28, V 4.90, Fe 0.29, Nb 0.05, Mn 0.03. Cr 0.02, Si 0.05, Sn <0.05, Mo <0.03, Cu <0.02, Zr 0.01, and Ti balance (all in wt.%). Wire brushing (WB) was carried out using a 64-mm-diameter circumferential brush with 0.3-mm-diameter stainless steel wires. The whole surface of a 10 cm × 2 cm work piece was subjected to wire brushing. The sheet was fixed along the rolling direction and wire brushed for 45, 60, and 75 s. The wire brush was rotated at 12,000, 16,000, 21,000, and 27,000 revolutions per min (rpm), while a force of 2 kg was applied vertically to the surface of the sheets. Cross and lateral sections of the wire brushed samples were mounted, and then mechanically polished, followed by etching in an etchant composed of 2.5% HNO_3, 1.5% HF, and 96% distilled water. The phase composition of brushed surface was analyzed by XRD (Philips PW 1480) in $2\theta = 20–100^\circ$ range. The hardness profile was obtained using a scanning microhardness tester with a load of 10 N. Surface roughness and topography of AR and WB samples were characterized by scanning probe microscope (SPM, DME DS-95-50E)

2.3. Electrophoretic deposition of nano-HA particles on Ti–6Al–4V substrates

The suspension was prepared by adding 1 g of HA powders into 50 mL of absolute ethanol (Merck, USA). The addition of 1 g/L iodine (dispersant) to ethanol was resulted in positively charged particles. The prepared suspension was dispersed in a 50 kHz ultrasonic bath for 60 min, and then was immediately used for electrophoretic deposition (EPD) without further aging. The particle size distribution of powders in the suspension was analyzed by dynamic light scattering (Malvern ZEN 3600). All measurements of dynamic light scattering (DLS) were carried out with slurries containing a 0.4 g/L solid loading. Ti–6Al–4V substrate as the working electrode and 316 L stainless steel as the counter electrode were immersed in the suspension with a fixed distance of 10 mm. Prior to deposition, Ti–6Al–4V substrates were polished from 400 to 1200 grid SiC papers, then washed out with detergent and degreased with acetone, and finally passivated in a HF (100 mL/L)–HNO_3 (300 mL/L) solution. One side of the cathode was masked with a nonconducting tape. The surface area of the cathode was 1 cm^2. The EPD process was conducted for 60 s under a constant voltage of 30 V. After deposition, the green coatings were dried in air for 24 h at room temperature. Sintering of the coatings was carried out in an argon-purged atmosphere at 900 °C. The heating rate and cooling rate were the same (100 °C/h) and the dwell time was 1.5 h. The phase composition of coated surface was analyzed by XRD (Philips PW 1480), by scanning in $2\theta = 20–100^\circ$ range at a step size of 0.02° and a count time of 0.6 s. The micro-structural characterization and surface topography of the as-deposited sample was carried out by using SEM (Philips XL 30) and SPM (DME DS-95-50E), respectively. To investigate electrochemical corrosion behavior of coatings on Ti–6Al–4V with and without wire-brushing treatment, samples were embedded in cold-curing epoxy resin, exposing a surface area of 1 cm^2. Potentiodynamic polarization test in a corrected-SBF solution [32], open to air at 37.4 °C and at the physiological pH 7.40, was performed using AutoLab PGstat 30. The chemical composition of the employed SBF is given in Table 1. All potentials were measured with respect to a saturated calomel electrode. Two parallel graphite rods served as the counter

Table 1
Chemical composition of simulated body fluid employed in this study.

Ion	SBF (mM)	Blood plasma (mM)
Na^+	142.0	142.0
K^+	5.0	5.0
Mg_2^+	1.5	1.5
Ca_2^+	2.5	2.5
Cl^-	147.8	103.0
HCO_3^-	4.2	27.0
HPO_4^{2-}	1.0	1.0
SO_4^{2-}	0.5	0.5

electrode for current measurement. From the polarization curve, the corrosion parameters were evaluated by Tafel extrapolation method by VersaStudio v2.03 software. Bonding strengths of the sintered specimens were measured by using a pull-off adhesion tester (PosiTest, Defelsko). A ten millimeter diameter Al rod was glued onto the coated surface with epoxy resin as the hardener. The adhesive strength was then calculated as the tensile force per fracture area.

3. Results and discussion

3.1. Characterization of the synthesized nano-HA particles

Fig. 1 shows the X-ray diffraction pattern of nano-HA particles synthesized by precipitation method. The mean crystallite size (d) of the synthesized particles was calculated from XRD line-broadening measurement via Scherrer equation [33]:

$$d = \frac{0.94\lambda}{b\cos\theta} \tag{1}$$

where λ is the wavelength (Cu K_α), b the full width at half-maximum of the HA lines, and θ the diffraction angle. The size of crystallites varies from 20.9 to 31.8 nm for the (0 0 2) and (2 1 1) crystal planes, respectively (Table 2).

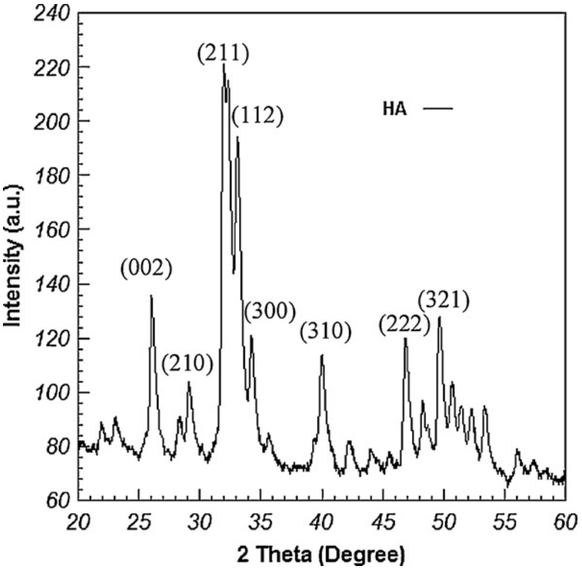

Fig. 1. XRD patterns for HA nanoparticles produced by precipitation method.

The fraction of crystalline phase (X_c) of the synthesized nano-HA particles was estimated by the following equation (Table 2) [34]:

$$X_C = \frac{1 - v_{112/300}}{I_{300}} \tag{2}$$

where I_{300} is the intensity of (3 0 0) diffraction peak and $v_{112/300}$ the intensity of the hollow between (1 1 2) and (3 0 0) diffraction peaks of HA.

The FTIR spectrum of HA sample is shown in Fig. 2. The wave numbers of functional groups that belong to nano-HA powders indicate PO_4^{3-} bands at 570, 602, 1047, and 1090 cm^{-1}. The water associated with HA appears at 1630 and 3423 cm^{-1}. The OH^- stretching vibration is observed at 632 and 3572 cm^{-1}. The blunt and smooth peaks at 1470 and

Table 2
XRD and DLS analyses of HA nanoparticles synthesized by precipitation method.

XRD analysis						DLS analysis	
Crystallite size for planes, nm					Crystallinity, %	Mean agglomerate size, nm	Particle distribution width, nm
(0 0 2) 20.9	(2 1 1) 31.8	(1 1 2) 28.4	(3 1 0) 24.9	(2 2 2) 22.2	72	182.5	36.52

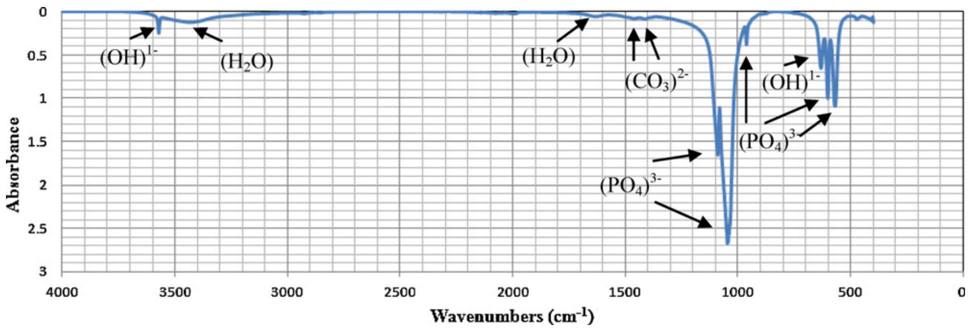

Fig. 2. The FTIR spectra of HA nanoparticles synthesized by precipitation method.

1420 cm^{-1}, are attributed to CO_3^{2-} ions which might be the result of the absorption of atmospheric CO_2 on the surface of HA particles [35]. These peaks are very weak which implies very low carbonate content of the sample.

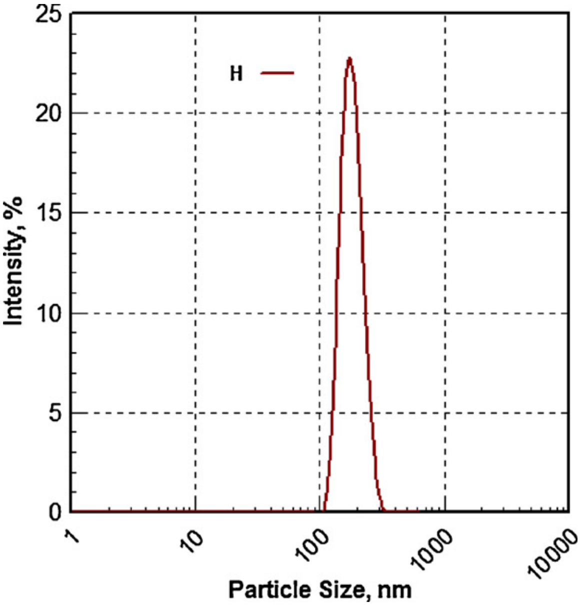

Fig. 3. Particle size distribution of HA nanoparticles in the ethanol-based suspension by DLS method.

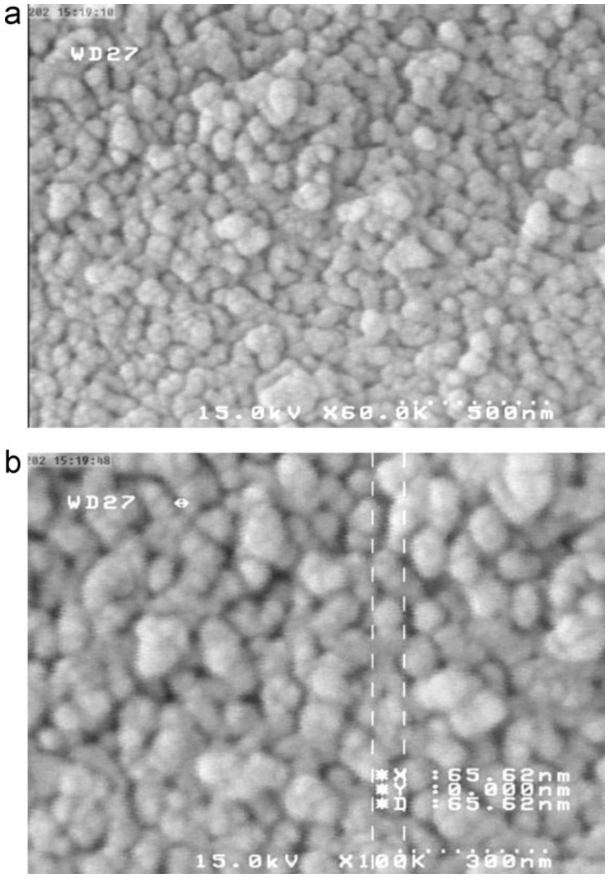

Fig. 4. FE-SEM images of nano-HA samples synthesized by precipitation method: the magnification of (a) ×60,000 and (b) ×100,000.

Fig. 3 illustrates the agglomerate size distribution of nano-HA particles in an ethanol-based suspension obtained from DLS analysis. The mean agglomerate size and the range of particle size distribution are 182.5 nm and ∼106–336 nm, respectively (Table 2). FE-SEM micrographs of the nano-HA particles are presented in Fig. 4. The particles possess spherical morphology with the size of approximately 65 nm. The contradiction between the results obtained from the particle

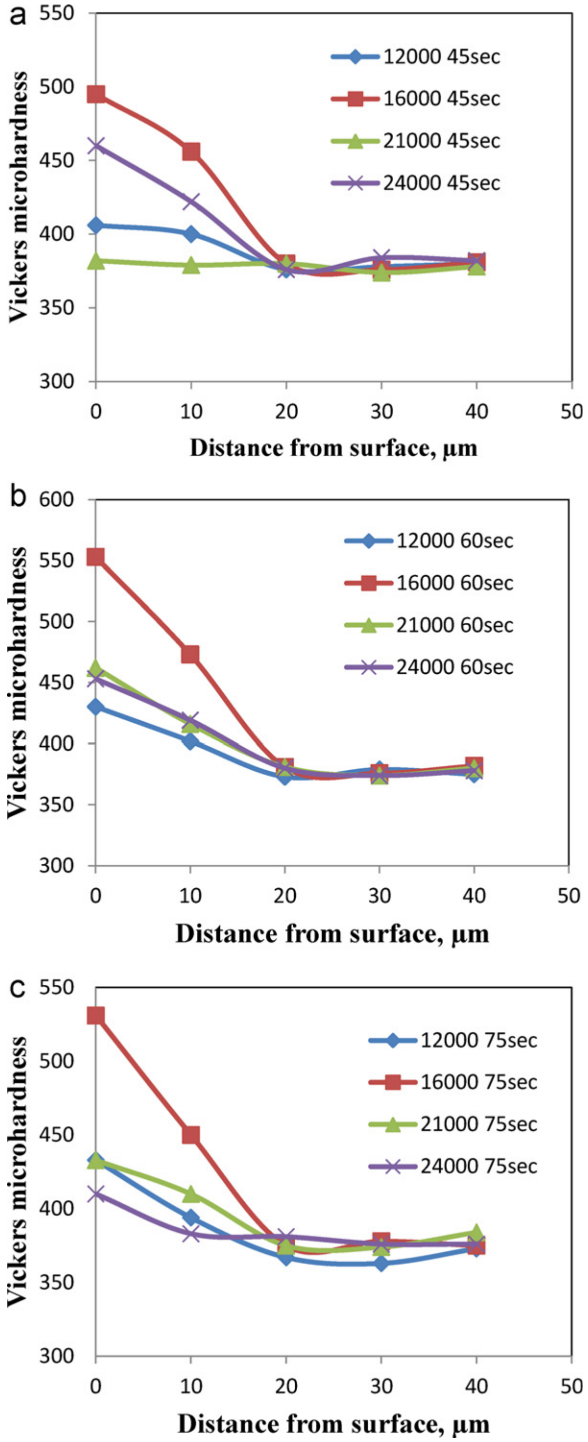

Fig. 5. The microhardness profile of WB samples at different rotational speeds (rpm) after 45 (a), 60 (b), and 75 s (c) versus the distance from the surface.

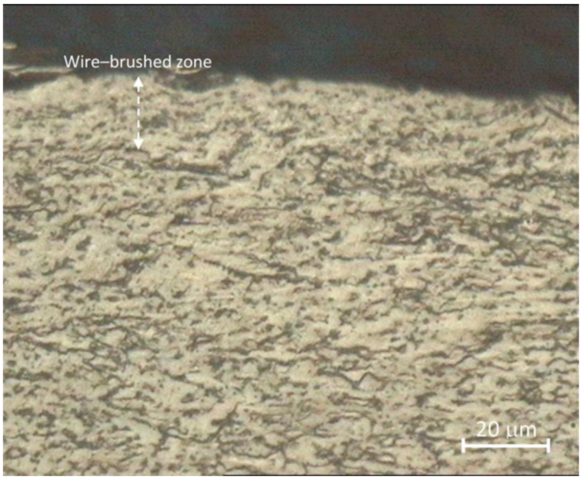

Fig. 6. The microstructural evolution from the wire-brushed layer on the surface.

size analyzer (Fig. 3) and those obtained by FE-SEM stems from the nature of dynamic light scattering (DLS) method. Furthermore, it is likely that a partial agglomeration of very fine particles occurred at the step of preparing an ethanol-based suspension [36].

3.2. Wire brushing of Ti–6Al–4V substrates

Fig. 5 presents the microhardness profile of the samples versus the distance from the wire-brushed surface at different rotational speeds and times. According to Fig. 5a–c, a maximum increase in microhardness (around 48%) can be observed in severe deformed layers at a rotational speed of 16,000 rpm after 60 s. Besides, the thickness of the formed wire-brushed layer may reach to 20 μm (Fig. 6) which is in agreement with Fig. 5. A decrease in grain size (Fig. 6) accompanied by a considerable increment in hardness (Fig. 5), is observed along the mentioned depth.

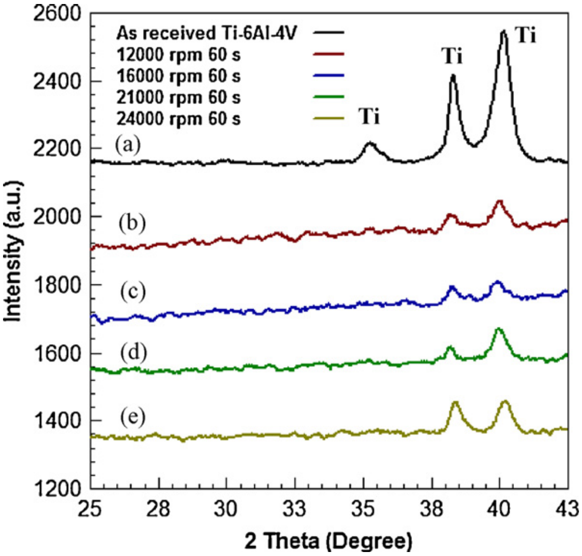

Fig. 7. X-ray diffraction patterns of (a) AR and WB samples at rotational speed of 12,000 (b), 16,000 (c), 21,000 (d), and 24,000 rpm (e) after 60 s.

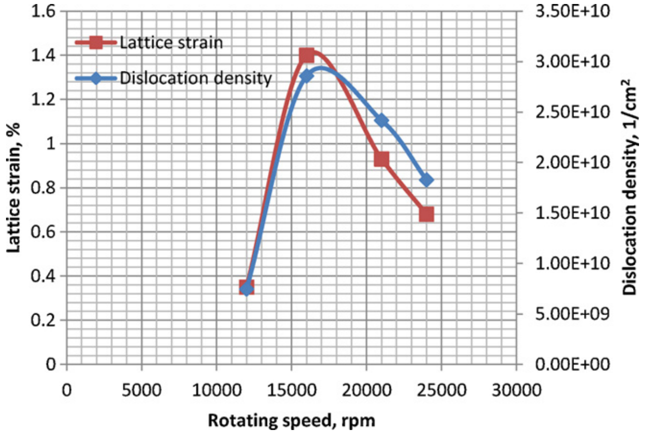

Fig. 8. Lattice strain and dislocation density obtained from Eqs. (3) and (4) against rotational speed of WB treatment for 60 s.

X-ray patterns of as-received (AR) and wire-brushed (WB) samples at different rotational speeds are illustrated in Fig. 7. X-ray line broadening analysis by the Williamson–Hall equation [35] was employed to characterize the WB samples in terms of lattice strain ($\varepsilon_{\mathrm{rms}}$) and dislocation density (ρ_D) [37]:

$$\varepsilon_{\mathrm{rms}} = \left(\frac{2}{\pi}\right)^{1/2}\left(\frac{\Delta d}{d_0(hkl)}\right) \tag{3}$$

$$\rho_D = 2\sqrt{3}\frac{\varepsilon_{\mathrm{rms}}}{tb} \tag{4}$$

where Δd is the difference between calculated and observed inter-planar spacing, $d_0(h\,k\,l)$ the observed inter-planar spacing, t the crystallite size, and b the burgers vector of dislocation. The effect of WB on lattice strain and dislocation density is depicted in Fig. 8 for different rotational speeds. As can be seen, both the lattice strain and dislocation density reach to their maximum values at 16,000 rpm; this result conforms to the broader Ti peaks in the case of 16,000 rpm rotational speed (Fig. 7). It is worthy of note that the structural defects, such as dislocations, can form dense regions and/or untidy clusters into the grains and pile-up the grain boundaries (GBs); [36]. On the other hand, the severe plastic deformation (SPD) caused by WB (up to 16,000 rpm) leads to an increase in lattice strain and consequently, it brings a deformed lattice with high dislocation density (Fig. 8). However, WB at higher rotational speeds (>16,000 rpm) results in decreasing lattice strain and dislocation density due to softening of the GBs.

The AFM images presented in Fig. 9 show that after WB treatment the grain size decreases drastically. The presence of such grain-refined layer on the surface of WB sample confirms the results illustrated in Figs. 5 and 8. During a sever plastic deformation of Ti–6Al–4V alloy, the occurrence of dynamic recrystallization (DRX) is the most probable restoration mechanism [37]. The severity of plastic deformation results in the formation of dislocation tangle zones close to the grain boundaries. Then, annihilation of dislocations leads to subgrain formation and finally new dislocations-free grains are produced with high misorientations [38].

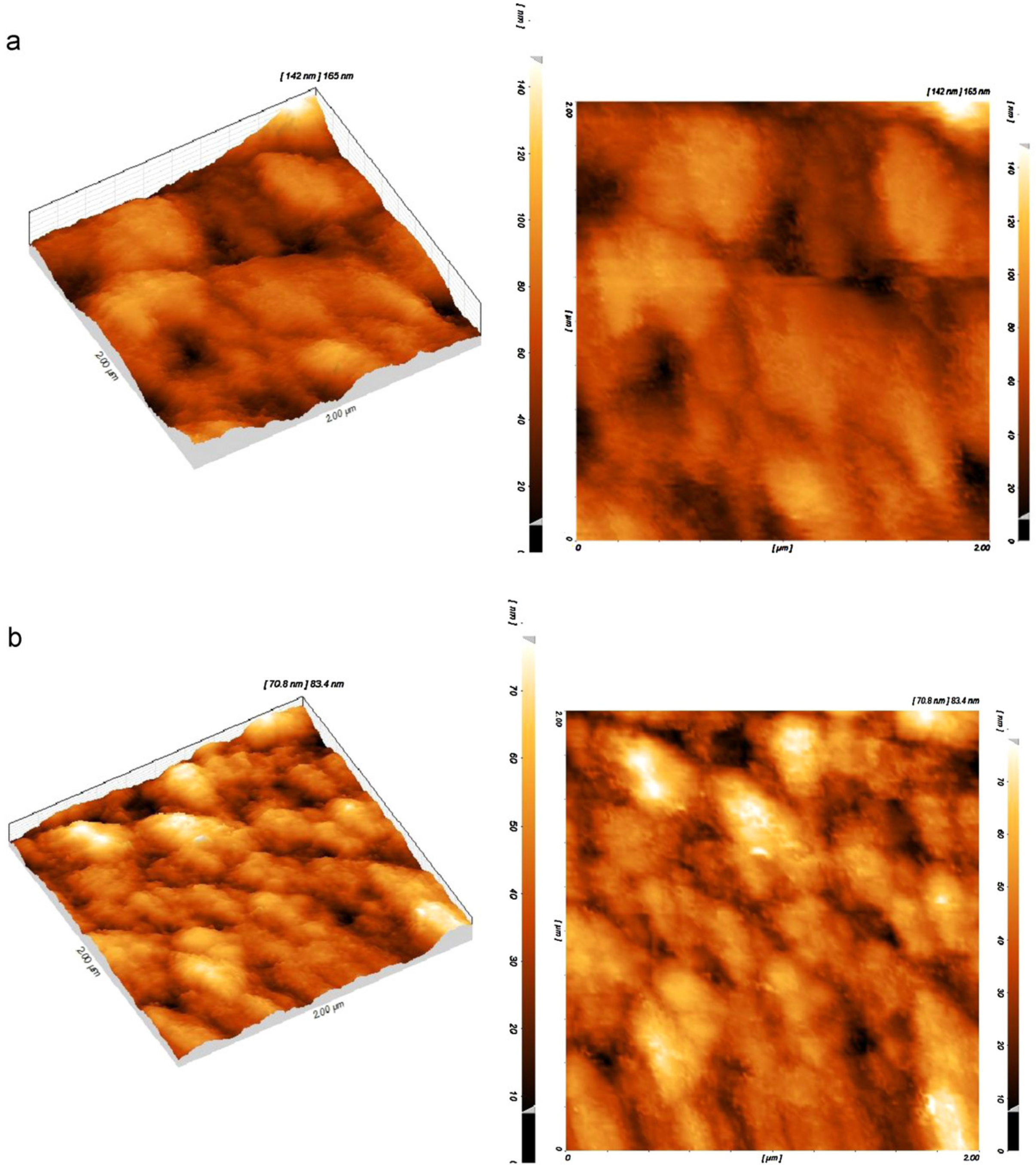

Fig. 9. AFM images of (a) the AR surface and (b) WB sample at 16,000 rpm after 60 s.

Fig. 10 shows that the area roughness parameters (i.e. S_a and S_q) of the WB samples are ~60% higher than those of AR sample. In addition, the characterization of the surface roughness is very important for biomedical application where an appropriate roughened surface is highly desirable due to its higher bonding strength with the coating [29].

3.3. Effect of wire brushing on the nano-HA coating

Fig. 11 illustrates XRD spectra of electrophoretically as-deposited and sintered samples. The patterns reveal that Ti peaks of the WB sample are much broader than those of AR sample due to its refined microstructure (Fig. 5). Also, SEM micrograph of the nano-HA coated on WB sample shown in Fig. 12 indicates that the coated surface is composed of HA nanoparticles with the size of ~76 nm. The values of bonding strength for the coated samples are presented in Fig. 13. The data shows that bonding strength of the WB sample is 2 times higher than that of as-received Ti–6Al–4V. Moreover, the bonding strength of WB sample is higher than that of AR sample (~24 MPa); this value is higher than those reported for HA coated samples (7–11 MPa) [39]. This enhancement in bonding strength of the HA coating stems from the surface roughening and the mechanical interlocking induced by wire

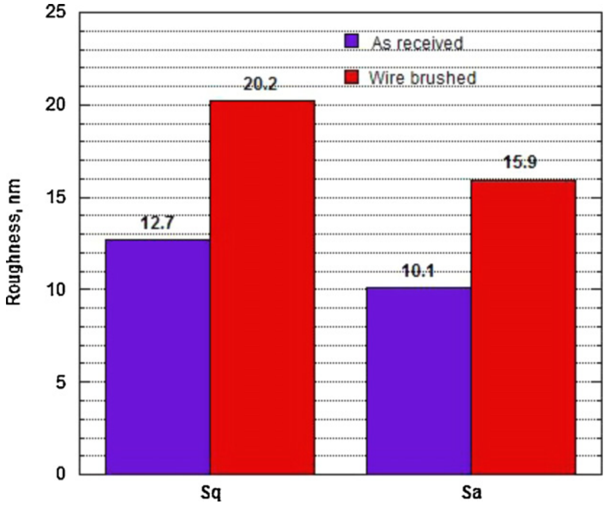

Fig. 10. Surface roughness of the AR and WB samples at 16,000 rpm after 60 s.

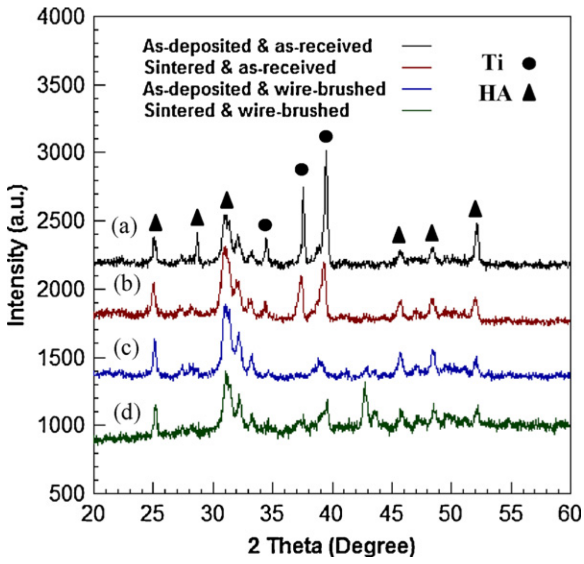

Fig. 11. X-ray diffraction patterns of as-deposited (a,c) and sintered (b,d) samples; (a,b) AR and (c,d) WB at 16,000 rpm after 60 s samples.

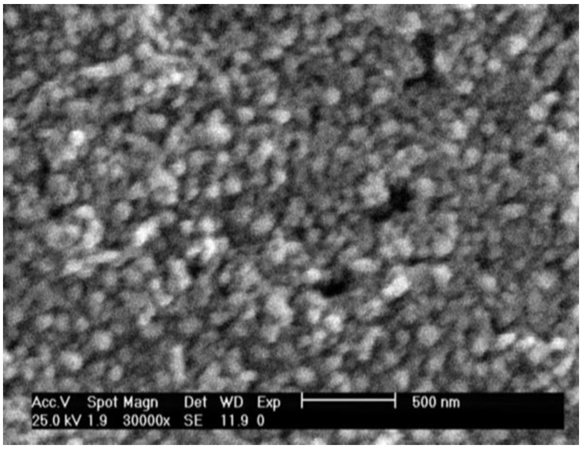

Fig. 12. SEM micrograph showing the surface morphology of as-deposited nano-HA on the WB sample.

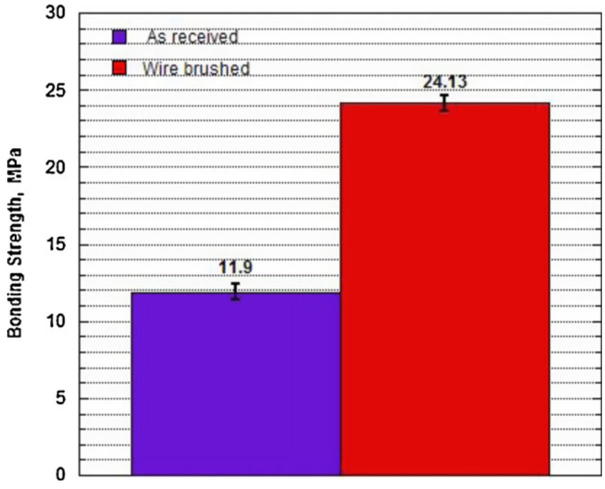

Fig. 13. Bonding strength of coatings on the AR and WB at 16,000 rpm after 60 s samples.

brushing pretreatment (Fig. 9). Fig. 14 displays AFM 3D images of the coating surface for AR and WB samples. The existence of a lower degree of porosity in HA coating on WB sample (about one-half the as-received sample) indicates the higher strength of bonding between coating and substrate.

The potentiodynamic polarization curves of the coated AR and WB samples in a corrected-SBF solution are depicted in Fig. 15. The corrosion parameters, extracted from polarization curves using Tafel least square fitting method, are listed in Table 3. Additionally, the polarization resistance (R_p) is estimated by the use of Stern–Geary equation $(R_p((\beta_a \times \beta_c)/(2.303(\beta_a + \beta_c)))(1/I_{corr}))$ [40]. The results corresponding to WB sample imply a significant decrease in the corrosion current density (I_{corr}), and an increase in the corrosion potential (E_{corr}), linear polarization resistance (R_p) and corrosion rate. By implementation of WB treatment, the nano-HA coating becomes more compact due to the mechanical interlocking of the particles at the interface. The HA layer acts as a barrier to the penetration/transport of chloride ions and water molecules through the coating, transport of ions the coating, and hinders the subsequent electrochemical reactions at the interface of HA and Ti–6Al–4V [39]. In addition, the corrosion rate of WB sample is lower in compared to the AR substrate which is

Table 3
Electrochemical corrosion parameters of coated AR and WB at 16,000 rpm after 60 s samples.

Sample	E_{corr} (mV)	I_{corr} (μA/cm^2)	β_a (V/decade)	β_c (V/decade)	R_p (Ω cm^2)	Corrosion rate (mm/year) $\times 10^{-2}$
Coated as-received	12.029	0.151	0.20	0.18	517,609	0.171
Coated wire-brushed	28.280	0.075	0.29	0.28	827,653	0.085

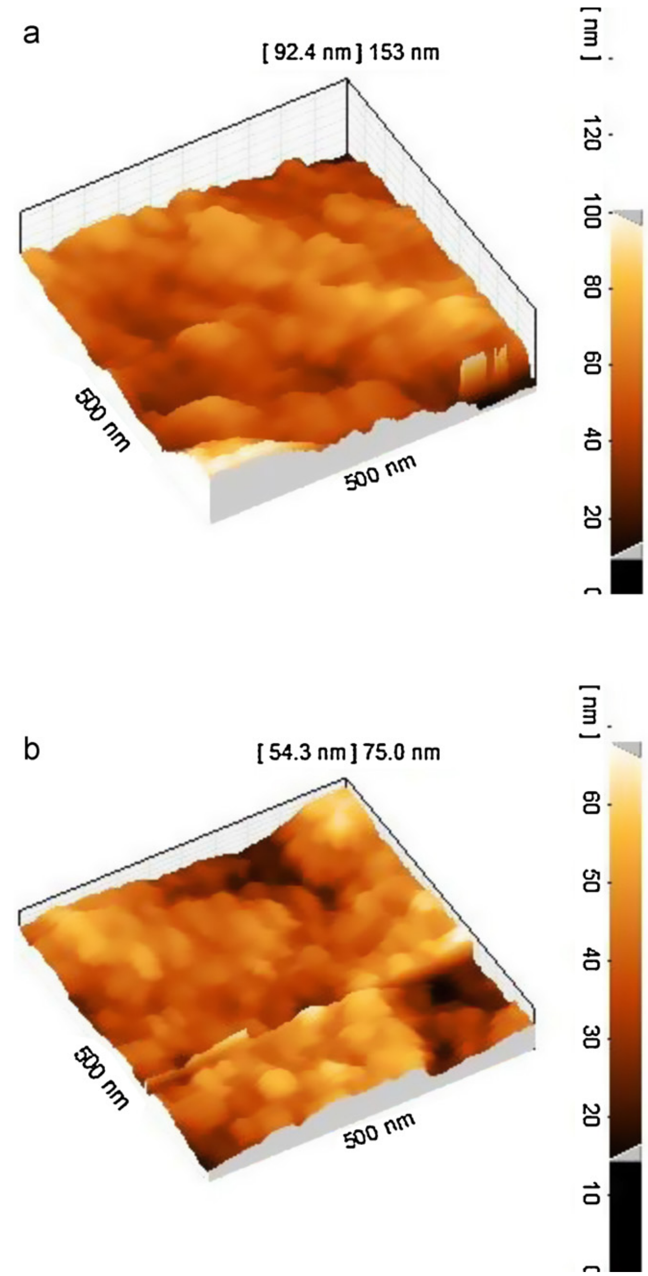

Fig. 14. AFM 3D images of as-deposited (a) AR and (b) WB samples at 30 V after 60 s.

because of the presence of much smaller pores in the deposited layer (Fig. 14).

4. Conclusions

In the present study, the wire brushing (WB) as a surface modification treatment, was performed on Ti–6Al–4V substrate to improve the nano-HA coatings. The chemical precipitation method was used to synthesize nano-HA powders with the size of 65 nm. The optimum WB parameters, including the rotational speed of 16,000 rpm and the time of 60 s, were obtained from microhardness and roughness analyses. The cathodic electrophoretic deposition of nano-HA particles in ethanol-based suspension was carried out on AR and WB specimens at constant voltage of 30 V after 60 s. It was found that WB process leads to an enhancement in the surface roughening which could effectively improve the bonding strength between coating and substrate. The electrochemical corrosion behavior of the nano-HA coatings in SBF solution at 37.8 °C was investigated by means of potentiodynamic polarization test. The results imply prior-wire brushing on Ti–6Al–4V substrates significantly decreases the corrosion current density, and increases the corrosion potential, linear polarization resistance and corrosion rate.

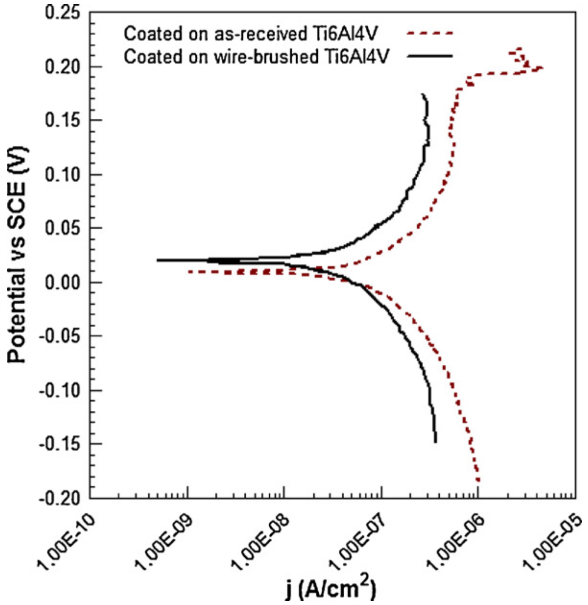

Fig. 15. Potentiodynamic polarization curves of nano-HA coated samples; the AR and WB at 16,000 rpm after 60 s samples in the simulated body fluid at 37 °C.

References

[1] M. Geetha, A.K. Singh, R. Asokamani, A.K. Gogia, Ti based biomaterials, the ultimate choice for orthopaedic implants–A review, Prog. Mater. Sci. 54 (2009) 397–425.

[2] S.R. Paital, N.B. Dahotre, Calcium phosphate coatings for bio-implant applications: materials, performance factors, and methodologies, Mater. Sci. Eng. R 66 (2009) 1–70.

[3] S. Sathish, M. Geetha, S.T. Aruna, N. Balaji, K.S. Rajam, R. Asokamani, Studies on plasma sprayed bi-layered ceramic coating on bio-medical Ti–13Nb–13Zr alloy, Ceram. Int. 37 (2011) 1333–1339.

[4] A. Dey, S.K. Nandi, B. Kundu, C. Kumar, P. Mukherjee, S. Roy, A.K. Mukhopadhyay, M.K. Sinha, D. Basu, Evaluation of hydroxyapatite and β-tri calcium phosphate microplasma spray coated pin intra-medullary for bone repair in a rabbit model, Ceram. Int. 37 (2011) 1377–1391.

[5] I. Sopyan, S. Ramesh, N.A. Nawawi, A. Tampieri, S. Sprio, Effects of manganese doping on properties of sol–gel derived biphasic calcium phosphate ceramics, Ceram. Int. 37 (2011) 3703–3715.

[6] A. Yelten, S. Yilmaz, F.N. Oktar, Sol–gel derived alumina–hydroxyapatite–tricalcium phosphate porous composite powders, Ceram. Int. (2011), doi:10.1016/j.ceramint.2011.11.032.

[7] H. Li, Z. Guo, B. Xue, Y. Zhang, W. Huang, Collagen modulating crystallization of apatite in a biomimetic gel system, Ceram. Int. 37 (2011) 2305–2310.

[8] D. Wei, Y. Zhou, Preparation, biomimetic apatite induction and osteoblast proliferation test of TiO_2-based coatings containing P with a graded structure, Ceram. Int. 35 (2009) 2343–2350.

[9] T.R. Rautray, R. Narayanan, K.H. Kim, Ion implantation of titanium based biomaterials, Prog. Mater. Sci. 56 (2011) 1137–1177.

[10] C. Kaya, Electrophoretic deposition of carbon nanotube-reinforced hydroxyapatite bioactive layers on Ti–6Al–4V alloys for biomedical applications, Ceram. Int. 34 (2008) 1843–1847.

[11] S. Subramanian, D. MubarakAli, N. Thajuddin, Fabrication of corrosion resistant, bioactive and antibacterial silver substituted hydroxyapatite/titania composite coating on Cp Ti, Ceram. Int. 38 (2012) 731–740.

[12] A.R. Boccaccini, S. Keim, R. Ma, Y. Li, I. Zhitomirsky, Electrophoretic deposition of biomaterials, J. R. Soc. Interface 7 (2010) S581–S613.

[13] S. Salman, O. Gunduz, S. Yilmaz, M.L. Öveçoğlu, R.L. Snyder, S. Agathopoulos, F.N. Oktar, Sintering effect on mechanical properties of composites of natural hydroxyapatites and titanium, Ceram. Int. 35 (2009) 2965–2971.

[14] D.Y. Lin, X.X. Wang, Preparation of hydroxyapatite coating on smooth implant surface by electrodeposition, Ceram. Int. 37 (2011) 403–406.

[15] C. Soundrapandian, S. Bharati, D. Basu, S. Datta, Studies on novel bioactive glasses and bioactive glass-nano-Hap composites suitable for coating on metallic implants, Ceram. Int. 37 (2011) 759–769.

[16] P.C. Rath, L. Besra, B.P. Singh, S. Bhattacharjee, Titania/hydroxyapatite bi-layer coating on Ti metal by electrophoretic deposition: characterization and corrosion studies, Ceram. Int. (2012), doi:10.1016/j.ceramint.2011.12.026.

[17] O. Albayrak, O.E. Atwani, S. Altintas, Hydroxyapatite coating on titanium substrate by electrophoretic deposition method: effects of titanium dioxide inner layer on adhesion strength and hydroxyapatite decomposition, Surf. Coat. Technol. 202 (2008) 2482–2487.

[18] L. Mohan, D. Durgalakshmi, M. Geetha, T.S.N. Sankara Narayanan, R. Asokamani, Electrophoretic deposition of nanocomposite ($HAp + TiO_2$) on titanium alloy for biomedical applications, Ceram. Int. (2012), doi:10.1016/j.ceramint.2011.12.056.

[19] M. Wei, A.J. Ruys, M.V. Swain, B.K. Milthorpe, C.C. Sorrell, Hydroxyapatite-coated metals: interfacial reactions during sintering, J. Mater. Sci. Mater. 16 (2005) 101–106.

[20] D. Jianxin, L. Taichiu, Surface integrity in electro-discharge machining, ultrasonic machining, and diamond saw cutting of ceramic composites, Ceram. Int. 26 (2000) 825–830.

[21] S. Kumar, R. Singh, T.P. Singh, B.L. Sethi, Surface modification by electrical discharge machining: A review, J. Mater. Process. Technol. 209 (2009) 3675–3687.

[22] B. Podgornik, J. Jerina, Surface topography effect on galling resistance of coated and uncoated tool steel, Surf. Coat. Technol. 206 (2012) 2792–2800.

[23] A.M. Awad, E.A. Ghazy, S.A. Abo El-Enin, M.G. Mahmoud, Electropolishing of AISI-304 stainless steel for protection against SRB biofilm, Surf. Coat. Technol. (2012), doi:10.1016/j.surfcoat.2011.11.046.

[24] H. Carreon, S. Barriuso, G. Barrera, J.L. González-Carrasco, F.G. Caballero, Assessment of blasting induced effects on medical 316 LVM stainless steel by contacting and non-contacting thermoelectric power techniques, Surf. Coat. Technol. 206 (2012) 2941–2946.

[25] L. O'Neill a, C. O'Sullivan, P. O'Hare, L. Sexton, F. Keady, J. O'Donoghue, Deposition of substituted apatites onto titanium surfaces using a novel blasting process, Surf. Coat. Technol. 204 (2009) 484–488.

[26] L. Pazosa, P. Corengia, H. Svoboda, Effect of surface treatments on the fatigue life of titanium for biomedical applications, J. Mech. Behav. Biomed. 3 (2010) 416–424.

[27] C. Leinenbach, D. Eifler, Fatigue and cyclic deformation behaviour of surface-modified titanium alloys in simulated physiological media, Biomaterials 27 (2006) 1200–1208.

[28] M. Multigner, E. Frutos, C.L. Mera, J. Chao, J.L. González-Carrasco, Interrogations on the sub-surface strain hardening of grit blasted Ti–6Al–4V alloy, Surf. Coat. Tech. 203 (2009) 2036–2040.

[29] C.Y. Zheng, F.L. Nie, Y.F. Zheng, Y. Cheng, S.C. Weic, R.Z. Valiev, Enhanced in vitro biocompatibility of ultrafine-grained titanium with hierarchical porous surface, Appl. Surf. Sci. 257 (2011) 5634–5640.

[30] B.D. Hahna, D.S. Park, J.J. Choi, J. Ryu, W.H. Yoon, J.H. Choi, J.W. Kim, Y.L. Cho, C. Park, H.E. Kim, S.G. Kim, Preparation and in vitro characterization of aerosol-deposited hydroxyapatite coatings with different surface roughnesses, Appl. Surf. Sci. 257 (2011) 7792–7799.

[31] P. O'Hare, B.J. Meenan, G.A. Burke, G. Byrne, D. Dowling, J.A. Hunt, Biological responses to hydroxyapatite surfaces deposited via a co-incident microblasting technique, Biomaterials 31 (2010) 515–522.

[32] T. Kokubo, Bioactive glass ceramics: properties and applications, Biomaterials 12 (1991) 155–163.

[33] B.D. Cullity, Elements of X-ray Diffraction, second ed., Addison-Wesley Publishing, 1977.

[34] E. Landi, A. Tampieri, G. Celotti, S. Sprio, Densification behaviour and mechanisms of synthetic hydroxyapatites, J. Eur. Ceram. Soc. 20 (2000) 2377–2387.

[35] P.N. Kumta, C. Sfeir, D.H. Lee, D. Olton, D. Choi, Nanostructured calcium phosphates for biomedical applications: novel synthesis and characterization, Acta Biomater. 1 (2005) 65–83.

[36] R. Xu, Progress in nanoparticles characterization: sizing and zeta potential measurement, Particuology 6 (2008) 112–115.

[37] Z. Guo, A.P. Miodownik, N. Saunders, J.P. Schillé, Influence of stacking-fault energy on high temperature creep of alpha titanium alloys, Scr. Mater. 54 (2006) 2175–2178.

[38] M. Hoseini, M.H. Pourian, F. Bridier, H. Vali, J.A. Szpunar, P. Bocher, Thermal stability and annealing behaviour of ultrafine grained commercially pure titanium, Mater. Sci. Eng. A 532 (2012) 58–63.

[39] C.T. Kwok, P.K. Wong, F.T. Cheng, H.C. Man, Characterization and corrosion behavior of hydroxyapatite coatings on Ti6Al4V fabricated by electrophoretic deposition, Appl. Surf. Sci. 255 (2009) 6736–6744.

[40] M. Stern, A.L. Geary, Electrochemical polarization: I. A theoretical analysis of the shape of polarization curves, J. Electrochem. Soc. 104 (1957) 56–63.